



ISSN: 2785-2997

# Journal of Human, Earth, and Future

Vol. 6, No. 1, March, 2025



## *Ganoderma* Disease in Oil Palm Trees Using Hyperspectral Imaging and Machine Learning

Chee Seng Kwang<sup>1,2</sup>, Siti Fatimah Abdul Razak<sup>1\*</sup>, Sumendra Yogarayan<sup>1</sup>,  
M. Z. Adli Zahisham<sup>2</sup>, Tze Huey Tam<sup>2</sup>, M. K. Anuar Mohd Noor<sup>2</sup>, Haryati Abidin<sup>3</sup>

<sup>1</sup> Faculty of Information Science and Technology, Multimedia University, Melaka 75450, Malaysia.

<sup>2</sup> iRadars Sdn Bhd, Jalan Eco 1, Zon Industri Ayer Keroh Baru, Melaka 75450, Malaysia.

<sup>3</sup> Geoinformatics Unit, FGV R&D Sdn Bhd, FGV Innovation Centre, PT23417, Lengkok Teknologi, Negeri Sembilan, Malaysia.

Received 10 September 2024; Revised 17 February 2025; Accepted 25 February 2025; Published 01 March 2025

### Abstract

The oil palm industry is one of the main contributors to the Malaysian national economy. However, the industry faces the challenge of *Ganoderma* infection, a destructive disease affecting oil palm trees that causes base stem rot (BSR). To address this issue, a novel method is proposed for detecting *Ganoderma* disease in oil palm trees by combining hyperspectral imaging and machine learning techniques. In this paper, four different classifiers, such as Support Vector Machine (SVM), Random Forest (RF), Multilayer Perceptron (MLP), and Decision Tree (DT), were trained on a tabular dataset generated by clustering spectral signatures of each pixel in the hyperspectral image. The evaluation results show that the MLP model showed 100% accuracy, sensitivity, and specificity in distinguishing between healthy and infected trees. SVM with radial basis function (RBF) and polynomial kernels show the second highest performance, attaining 91.67% accuracy, 83.33% sensitivity, and 100% specificity. Before training on classifiers, a feature-based band alignment technique is developed to overcome the hyperspectral image misalignment issue and ensure the accuracy of the spectral data. The developed band alignment significantly improved spectral coherence across the adjacent bands, as proved by enhanced Root Mean Squared Error (RMSE), Pearson Correlation Coefficient (PCC), and Normalized Mutual Information (NMI) values. Additionally, the developed background subtraction method effectively extracted the tree pixels from the background, resulting in a high precision score of 93.99%. Future research will focus on collecting more data, incorporating temporal information for disease stage classification, and implementing a more robust machine learning (ML) model for performance enhancement. Overall, this research shows the great potential of hyperspectral imaging for accurate detection of *Ganoderma* disease in oil palm plantations.

**Keywords:** *Ganoderma*; Basal Stem Rot; Oil Palm; Hyperspectral.

## 1. Introduction

The oil palm tree is a highly agriculturally valuable crop because it can provide three to four times more edible oil than soybean, sunflower, and rapeseed oil, measured in oil per hectare [1]. Oil palm is recognized as a high-yield crop, as it produces the same amount of oil while requiring less agricultural land than other oil crops. Besides edible oil, oil palms can also produce biodiesel, tocotrienols, animal feed, and various types of palm-related products. In Malaysia, the world's second-largest producer after Indonesia [2], oil palm is used for domestic consumption and export, making

\* Corresponding author: [fatimah.razak@mmu.edu.my](mailto:fatimah.razak@mmu.edu.my)

<http://dx.doi.org/10.28991/HEF-2025-06-01-05>

➤ This is an open access article under the CC-BY license (<https://creativecommons.org/licenses/by/4.0/>).

© Authors retain all copyrights.

it one of the main contributors to the country's economy. According to statistics, in 2022, Malaysia's export revenue from oil palm-related products reached RM82.49 billion, which increased by 27.7% compared to the previous year [3]. Therefore, it is essential to secure the health and productivity of these oil palm plantations. However, the oil palm industry faces a growing threat of pathogens named *Ganoderma Boninense* infection.

*Ganoderma Boninense* causes basal stem rot (BSR) disease [4], which is one of the most destructive diseases in oil palm [5]. It causes significant yield losses, estimated at up to 4.3 tons per hectare of fresh fruit bunches [6] and USD 500 million annually [7]. The infection damages the basal stem, disrupting water and nutrient uptake, thus impacting plantation productivity [8]. In recent years, research has shown that the disease is mainly spread to other trees via Basidiospores (spores) through the air or other types of transmission medium [9-11]. Therefore, treating or controlling infected trees is essential before the *Ganoderma* fruit body matures. However, infected trees show no apparent symptoms in the early stage of infection and only show significant foliage symptoms until it is developed by 60% to 70% [6]. This makes disease control difficult to perform early detection.

Traditionally, visual symptom observation is the most common way to detect *Ganoderma* disease by identifying significant foliar symptoms, such as mycelium or *Ganoderma* fruit bodies. This approach requires many experienced experts to perform the detection, which is time-consuming to cover a large plantation area [12], and detecting early infection is impossible. The second approach uses laboratory-based methods such as *Ganoderma* selective medium (GSM), polymerase chain reaction (PCR), and polyclonal antibodies (PABs), which have been developed to improve detection accuracy and early detection capabilities significantly. However, laboratory detection requires a laboratory environment [13, 14] and a trunk sample, which is costly and complex and may cause tree injury and destruction [15, 16]. As a result, there is a growing need for more efficient, reliable, and less non-destructive detection methods to facilitate early intervention and mitigate the spread of *Ganoderma* disease.

In recent years, researchers have focused on the spectroscopic techniques for *Ganoderma* detection, including point-based measurements [17-23] and image-based approaches using multispectral or hyperspectral data [4, 7, 12, 15, 16, 24-32]; a key gap remains in effectively utilizing the rich information available in hyperspectral imagery for early-stage detection. The existing approaches, using both spatial and spectral features, may not be suitable for *Ganoderma* disease detection where spatial features are less informative because infected trees show symptomless till late infection [33]. Other approaches focus on individual band selection or vegetation indices [15, 32], potentially overlooking subtle spectral variations captured across multiple bands. While machine learning and deep learning methods [32] have been employed, these typically operate on a reduced set of bands, potentially discarding valuable information. This underscores the need for methods to effectively leverage hyperspectral data's full spectral information content for improved early-stage *Ganoderma* detection.

To address this gap, this research proposes a novel method for detecting *Ganoderma* disease in oil palm trees using frame-based hyperspectral imaging and a data-driven approach to spectral representation. A frame-based hyperspectral camera mounted on a UAV captures images of oil palm canopies. Unlike methods relying on spatial features, this study uses K-means clustering to group pixels based on spectral similarity, capturing subtle, disease-specific differences. The distribution of these clusters for each tree forms a spectral representation used to train and evaluate multiple machine learning classifiers: Support Vector Machine (SVM), Random Forest (RF), Multilayer Perceptron (MLP), and Decision Tree (DT), aiming to identify the most effective model for distinguishing healthy and infected trees. This approach seeks to leverage hyperspectral data's full spectral information content while remaining computationally efficient.

The following section is structured as follows: Section 2 provides a comprehensive review of the existing application of spectroscopic techniques in *Ganoderma* disease detection. Section 3 describes the methodology developed in this study, including a description of the data collection, hyperspectral image pre-processing steps (which include band alignment, denoising, and background subtraction), and the prediction process using machine learning. Section 4 presents the experimental results, focusing on evaluating the effectiveness of the band alignment and background subtraction techniques and comparing the performance of different classifiers. Finally, Section 5 summarizes the key findings, the system's limitations, and the future work for improvement.

## 2. Application of Spectroscopy in *Ganoderma* Disease Detection

Spectroscopic techniques have been widely used in detecting and monitoring plant diseases, including *Ganoderma* disease in oil palm trees. These techniques offer more rapid, less destructive, continuous methods than laboratory or human measurements. Also, spectroscopy techniques can effectively measure the organic object [15], monitoring the biochemical changes during the disease progression. This paper has deployed various spectroscopic techniques for *Ganoderma* disease detection, categorized into point-based and image-based measurements.

### 2.1. Point-Based Measurement

Point-based spectroscopy in this paper refers to obtaining spectral data from individual points or small regions of interest using point spectrometers or spectroradiometers, which can collect spectral information at a specific range of

wavelengths. The spectral information, also known as spectral signature, contains the biochemical and structural information of the measured point. *Ganoderma* disease could be identified by analyzing the spectral signatures between the healthy and *Ganoderma*-infected leaf tissue at various wavelengths.

Various approaches have been proposed and developed using statistical analysis and vegetation indices. For instance, Lelong et al. [18] utilized Partial Least Squares Discriminant Analysis (PLS-DA) to perform classification. Based on the result, they can obtain an impressive 92.6% accuracy, 100% sensitivity, and 97% specificity. Similarly, Shafri et al. [19] developed a modified vegetation index using the Mann-Whitney U Test and band ratio. They used these two methods to implement the various indices. Using a silhouette plot, they performed K-means clustering to calculate the Average Silhouette Width (ASW) to identify the best indices. The authors found that the index using the wavelengths 610.5 nm and 738 nm shows the potential for early disease detection. Further advancements were made by Izzuddin et al. [20], who developed new indices using wavelength ratios and modified simple ratios (MSR). The authors found that key ratios and indices were based on wavelengths 655 nm, 750 nm, 495.5 nm, and 477.5 nm.

Various approaches use machine learning (ML) to predict *Ganoderma* disease. For example, Liaghat et al. [21] utilized Principal Component Analysis (PCA) to reduce the dataset dimensions. They achieved a remarkable 97% accuracy rate without a false-negative rate using K-Nearest Neighbour (KNN). Similarly, Tan et al. [22] use PCA-reduced spectra to train a Decision Tree (DT) model and eventually achieve remarkable performance of 93.1% accuracy, 91.5% sensitivity, and 94.5% specificity. Ahmadi et al. [17] used an Artificial Neural Network (ANN) to perform classification, resulting in 83% and 100% accuracy in distinguishing healthy and early-stage infections using only green wavelengths.

The existing spectroscopic techniques have shown significant potential for detecting and monitoring *Ganoderma* disease in oil palm trees. Point-based measurements have provided valuable insights and high accuracy rates in disease detection. However, the data collection requires taking leaf samples from the tree, which can be destructive and time-consuming. Therefore, there is a need to explore image-based measurements for a more comprehensive and efficient approach. Table 1 summarizes the previous studies using point-based measurement approaches according to their types of sensors, inspection areas, used wavelengths, and methods.

**Table 1. Summary of the previous studies (point-based measurement)**

Author	Type of Sensors	Inspection Area	Used Wavelength Range	Method
Ahmadi et al. (2017) [17]	Spectroradiometer	Fronde Number 9 and 17	273–1100 nm	<ul style="list-style-type: none"> <li>Apply Artificial Neural Network (ANN) with different topologies and epochs.</li> </ul>
Lelong et al. (2009) [18]	Spectroradiometer	Oil Palm Canopy	450–1100 nm	<ul style="list-style-type: none"> <li>Apply Partial-Least-Square Discrimination Analysis (PLS-DA) on first-order and second-order derivative datasets.</li> </ul>
Shafri et al. (2009) [19]	Spectroradiometer	Fronde	300–1000 nm	<ul style="list-style-type: none"> <li>Use the Mann-Whitney U Test to identify significant and insignificant bands to develop new vegetation indices for <i>Ganoderma</i> disease detection.</li> <li>Plot K-means cluster to evaluate the developed indices using silhouette plots to measure the Average Silhouette Width (ASW).</li> </ul>
Izzuddin et al. (2017) [20]	Spectroradiometer	Leaflet of the seedling (First top and second top)	300–1000 nm	<ul style="list-style-type: none"> <li>Significant Wavelength Selection                             <ul style="list-style-type: none"> <li>Select wavelengths that displayed a statistically significant difference in reflectance between healthy and <i>Ganoderma</i>-infected oil palm seedlings.</li> <li>One-way analysis of variance (ANOVA) is used to analyse the first derivative of reflectance spectra and compare the groups using statistical tests.</li> </ul> </li> <li>Spectral Index Development                             <ul style="list-style-type: none"> <li>Use the Optimum Index Factor (OIF) to identify the most informative pairs of wavelengths from the statistically significant set.</li> <li>OIF is used to find the best combination of wavelengths that can be ratioed to produce spectral indices and used in wavelength ratio and Modified Simple Ratios (MSR).</li> </ul> </li> <li>Evaluation and Selection                             <ul style="list-style-type: none"> <li>Mann-Whitney U due to non-normal data to confirm that the indices showed significant differences between the healthy and infected seedling groups.</li> <li>ASW was used to evaluate how well each index separated the data into distinct clusters representing the different levels of <i>Ganoderma</i> infection.</li> </ul> </li> <li>Regression analysis to examine the correlation between the spectral indices and a measure of plant health using total Leaf Chlorophyll (TLC), expecting a solid correlation to indicate an index's ability to track disease severity.</li> </ul>
Liaghat et al. (2014) [21]	Spectroradiometer	Fronde Number 17	325–1040 nm	<ul style="list-style-type: none"> <li>Using several ML models for classification: Linear Discriminant Analysis (LDA), Quadratic Discriminant Analysis (QDA), KNN, and Naive Bayes (NB).</li> </ul>
Tan et al. (2023) [22]	Spectroradiometer	Leaves of the oil palm seedlings	900–1700 nm	<ul style="list-style-type: none"> <li>Using several ML models for classification: KNN, NB, SVM, and DT.</li> </ul>
Liaghat, et al. (2014) [23]	Fourier transform infrared spectrometer	Canopy	2.55–25.05 μm	<ul style="list-style-type: none"> <li>Using several ML models for classification: LDA, QDA, KNN, and NB.</li> </ul>

## 2.2. Image-Based Measurement

Image-based measurement in this paper refers to obtaining spatial and spectral information simultaneously from images using different types of sensors such as hyperspectral, multispectral, thermal, and more. This approach allows the researchers to analyze the information on the oil palm trees' spectral and physical structure. The camera can also be equipped on a drone or unnamed aerial vehicle (UAV), making the camera capable of capturing the entire tree canopy and monitoring the plantations at a larger scale. Because of these characteristics, it can provide non-destructive and efficient monitoring of *Ganoderma* disease in oil palm plantations.

Hermantoro et al. [24] applied Self-Organizing Maps (SOM) to detect BSR in oil palm trees on RGB images. The trained SOM algorithm achieves a prediction accuracy of 73.8%. Also, the authors found a positive correlation between the red band and disease severity, while the blue band shows the vice versa.

Thermal imaging leverages temperature differences in plant tissues caused by biological activities. Johari et al. [25] used a thermal camera to capture oil palm leaves and leveraged PCA features extracted from images to train an SVM model and achieve 80% prediction accuracy. Similarly, Hashim et al. [26] use the thermal camera to capture oil palm trunks and convert them to structured data by extracting the image to maximum, minimum, mean, median, and standard deviation temperature features. Random forest (RF) is trained using balanced data, achieved by applying random oversampling, resulting in a good overall accuracy of 87.10% specificity and 100% sensitivity using only maximum and minimum temperature features.

Multispectral imaging extends the analysis beyond the visible spectrum, capturing additional spectral bands that provide more detailed information about plant health. Izzuddin et al. [4] achieved a low accuracy of 41.4% and 0.2836 Kappa coefficient by training a Neural Network classifier using the NIR band dataset. Izzuddin et al. [12] trained a support vector machine (SVM), which resulted in an accuracy score of 91.8% with a combination of green, red, and near-infrared data. The authors agree that different types of bands could indicate the condition of the plant, such as the green band being sensitive to the leaf nitrogen and pigment. At the same time, the red band is sensitive to chlorophyll a and b content, and the red edge band is sensitive to plant stress and chlorophyll content. The NIR band is sensitive to the plant's water content, moisture, and biomass.

Wiratmoko et al. [27] used vegetation indices to identify and map *Ganoderma* infection levels in an oil palm plantation. Four vegetation indices were calculated: Simple Ratio (SR), Normalized Difference Vegetation Index (NDVI), Enhanced Vegetation Index (EVI), and Atmospherically Resistance Vegetation Index (ARVI) and compared to ground-truth data collected through manual inspection. The results showed that the SR index demonstrated the highest accuracy at 86.5%.

Other research also uses spectral bands and vegetation indices to improve the performance of detecting *Ganoderma* disease. For example, Ahmadi et al. [28] developed early detection of *Ganoderma* disease using multispectral imaging with red, green, and near-infrared (NIR) bands. Features are further extracted to Normalized Difference Vegetation Index (NDVI) and textural information from the grey-level co-occurrence matrix (GLCM). The spectral bands and extracted features fit into an SVM model. The result shows a 68.28% accuracy with a kappa coefficient of 0.57. The authors mentioned that the model has challenges in distinguishing mildly infected palms due to the subtle spectral reflectance differences at the early stages of infection, leading to some misclassification. Similarly, Wahyuni et al. [29] aim to develop a rapid and accurate detection of *Ganoderma* disease using multispectral imaging to train SVM and RF models with all spectral bands and extracted features such as Green Normalized Difference Vegetation Index (GNDVI), Soil Adjusted Vegetation Index (SAVI), Green Chlorophyll Index (CIgreen), NDVI, and SR. The result shows 93.55% accuracy on SVM and 84.42% on RF.

Handrian et al. [30] combine machine learning and Sentinel-2 multispectral imaging to identify basal stem rot disease in different severities. The Random Forest (RF) model was trained using ten bands of Sentinel-2 imagery. The model's performance shows 82% accuracy, 90.32% sensitivity, and 87.5% specificity. Similar to Ahmadi et al. [7], they combined multispectral imagery and artificial neural networks (ANNs) for the early detection of *Ganoderma* disease in oil palm using a modified RGB camera to capture green, red, and NIR bands. The result of the trained ANN showed an accuracy of 72.73% in differentiating between healthy palm trees. The study highlights the potential of this approach as a rapid, cost-effective method for large-scale disease monitoring in oil palm plantations.

Recent studies have explored hyperspectral imaging and deep learning for early and accurate detection of Basal Stem Rot (BSR) disease in oil palm trees. Hyperspectral cameras can capture narrow bandwidths like spectrometers or spectroradiometers while capturing spatial information like RGB or multispectral imagery. Azmi et al. [16] demonstrated combining hyperspectral and SVM classifiers for early detection of *Ganoderma*. They collected the images from oil palm seedlings and achieved 95% when using NIR bands for *Ganoderma* early detection. With the same images, Khairunniza-Bejo et al. [15] resulted in 94.8%, 97.6%, and 92.5% accuracy, sensitivity, and specificity, respectively, using a linear SVM model with a single NIR band. Furthermore, Yong et al. [31] explored the use of deep learning models using the same images, specifically VGG16 trained on hyperspectral data, revealing that VGG16 achieved the highest 91.93% accuracy, 89.26% sensitivity, and 94.32% specificity when trained with unsegmented images at 938 nm wavelength.

There is also research using hyperspectral imaging to capture oil palm trees. Lee et al. [33] proposed a Multilayer Perceptron (MLP) model that relies solely on spectral features to analyze hyperspectral images, achieving an 86.67% classification accuracy in differentiating BSR infection stages. Similarly, Kurihara et al. [32] employed a Random Forest

(RF) algorithm for BSR detection with UAV-based hyperspectral imagery. They introduced a novel concentric disk segmentation method to analyze reflectance spectra at the sub-plant scale. They identified a limited set of spectral bands within the red-edge region as highly informative for accurate classification.

Table 2 summarizes the previous studies using image-based measurement approaches according to their types of sensors, inspection areas, used wavelengths, and methods. In conclusion, image-based spectroscopic methods are invaluable for the non-destructive and efficient detection of *Ganoderma* disease in oil palm plantations. From simple RGB imaging analyzed with machine learning to sophisticated hyperspectral systems paired with deep learning models, these techniques offer a scalable solution for monitoring large areas. Furthermore, the development and application of UAV-based platforms enhance this scalability while allowing for a comprehensive assessment of individual tree health and detecting subtle spectral changes associated with early-stage infections. As technology advances, we can anticipate further refinements and applications of image-based spectroscopy for even more precise, efficient, and timely detection and management of *Ganoderma* disease.

**Table 2. Summary of the previous studies (image-based measurement)**

Author	Type of Sensors	Inspection Area	Used Wavelength Range	Method
Ahmadi et al. (2022) [7]	Multispectral	Tree Crown	Digital Camera with an external NIR filter.	<ul style="list-style-type: none"> <li>Artificial Neural Network (ANN) with an early stopping mechanism to avoid overfitting.</li> </ul>
Izzuddin et al. (2020) [12]	Multispectral	Capture tree crown by mounting the camera on the UAV	Multispectral Camera with four bands: Green, Red, Red Edge, and NIR.	<ul style="list-style-type: none"> <li>SVM with RBF.</li> </ul>
Khairunniza-Bejo et al. (2021) [15]	Hyperspectral	Canopy of the seedling	450–950 nm	<ul style="list-style-type: none"> <li>Using SVM models with different kernels: Linear, Quadratic, Cubic, Fine Gaussian, Medium Gaussian, and Coarse Gaussian.</li> <li>Five-fold cross-validation technique to evaluate the performance of the trained models.</li> </ul>
Azmi et al. (2020) [16]	Hyperspectral	Canopy of the seedling	450–950 nm	<ul style="list-style-type: none"> <li>Using SVM models with different kernels: Linear, Gaussian RBF, and Polynomial.</li> <li>Five-fold cross-validation technique to evaluate the performance of the trained models.</li> </ul>
Hermantoro et al. (2023) [24]	RGB	Canopy	N/A	<ul style="list-style-type: none"> <li>Apply the SOM model</li> </ul>
Johari et al. (2021) [25]	Thermal	Seedling Canopy by handheld the thermal camera	635 nm	<ul style="list-style-type: none"> <li>Using several ML models for classification: SVM, KNN, LDA, QDA.</li> </ul>
Hashim et al. (2021) [26]	Thermal	Tree Trunk	Detail refers to the specifications on the FLIR T260 IR thermal camera	<ul style="list-style-type: none"> <li>Under-sampling, oversampling or Synthetic Minority Oversampling (SMOTE) is performed to solve imbalanced data.</li> <li>Using several ML models for classification: NB, MLP, and RF.</li> <li>Using cross-validation (WEKA's K-fold) due to small sample size.</li> </ul>
Izzuddin et al. (2019b) [12]	Multispectral	Canopy	Multispectral Camera with red, green, blue, and NIR bands	<ul style="list-style-type: none"> <li>Using several ML models for classification: Maximum Likelihood, MD, and Neural Network (NN)</li> </ul>
Wiratmoko et al. (2018) [27]	Multispectral	Canopy	Multispectral Camera with blue, red, and NIR bands	<ul style="list-style-type: none"> <li>Prediction by Thresholding:                             <ul style="list-style-type: none"> <li>For a given palm, its index value is compared against the pre-defined thresholds.</li> <li>Assigned to associated infection level if the values are within the range.</li> </ul> </li> </ul>
Ahmadi et al. (2023) [28]	Multispectral	Canopy	<ul style="list-style-type: none"> <li>Multispectral Camera with red, green, and NIR bands</li> <li>Pleiades Satellite Image with Band 0 (0.43–0.55 um), Band 1 (0.50–0.62 um), Band 2 (0.59–0.71 um), and Band 3 (0.74–0.94 um)</li> </ul>	<ul style="list-style-type: none"> <li>Apply the SVM model</li> </ul>
Wahyuni et al. (2024) [29]	Multispectral	Canopy	3 Bands: Green, Red, and NIR	<ul style="list-style-type: none"> <li>Red, Green and NIR bands and five vegetation indices are used as input features to fit into two ML models for classification: RF and SVM.</li> </ul>
Handrian et al. (2022) [30]	Multispectral	Canopy	Sentinel-2	<ul style="list-style-type: none"> <li>Apply RF model</li> </ul>
Yong et al. (2022) [31]	Hyperspectral	Canopy of the seedling	450–950 nm	<ul style="list-style-type: none"> <li>Data augmentation on both sets: Rotation Horizontally, Vertical Flip, and Zoom.</li> <li>Train VGG16 for transfer learning using unsegmented images and Mask RCNN segmented images.</li> </ul>
Lee et al. (2022) [33]	Hyperspectral	Canopy	N/A	<ul style="list-style-type: none"> <li>Apply MLP model</li> </ul>
Kurihara et al. (2022) [32]	Multispectral	Canopy	460–780 nm Detail refers to [35]	<ul style="list-style-type: none"> <li>Apply RF model</li> </ul>
Win Kent et al. (2023) [34]	RGB	Canopy	N/A	<ul style="list-style-type: none"> <li>Applied rotations (90, 180, 270 degrees) and vertical flips to increase training data size and model robustness.</li> <li>Use a modified U-Net architecture with a Multi-Convolution Residual (M-CR) block.</li> </ul>

### 3. Methods

During the early stage of infection, the trees show no symptoms and look like healthy trees. The foliage symptoms show only when *Ganoderma* disease is developed up to 60% [6], such as yellowish fronds, fronds wilting, hanging small canopies, and more. Therefore, it is not ideal to include spatial features in disease detection. In this paper, the raw dataset of each tree pixel is flattened and clustered into several pixel classes. Then, the distribution of the clustered pixel classes is calculated and converted to a tabular dataset. The proposed method is shown in Figure 1. The captured hyperspectral images require preprocessing before identifying affected trees. The processes involve band alignment, denoising, and background subtraction.

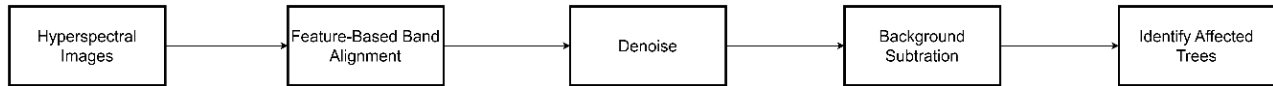


Figure 1. Proposed method

#### 3.1. Dataset

In this study, oil palm trees at the Palong Timur site in Johor, Malaysia, were surveyed. Seven blocks were defined for data collection, which occurred in August 2023 between 11 a.m. and 12 p.m. under sunny, clear conditions. Field evaluations were conducted by several experienced oil palm disease specialists from Felda Global Ventures (FGV). The selection of experts by FGV was meticulously based on their extensive and specialized experience in the precise identification of oil palm *Ganoderma* fruiting bodies, which spans over a decade. Additionally, these experts possess significant expertise in systematically collecting, analyzing, and managing *Ganoderma*-related data. Their experience is further reinforced by their comprehensive work conducting thorough *Ganoderma* data censuses across multiple FGV estates in Malaysia. The trees are categorized as healthy and infected based on the visual symptoms shown in Figure 2. Healthy oil palm trees refer to non-*Ganoderma*-infected oil palm trees. Oil palm trees with symptoms of white mycelium in the stem bark or brittle wood or the presence of *Ganoderma* fruit bodies are identified as infected oil palm trees.

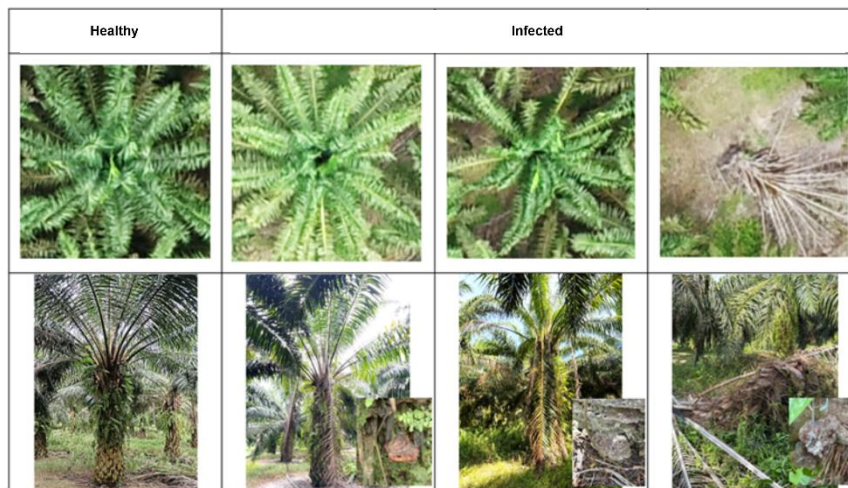


Figure 2. *Ganoderma* infection category in oil palm tree (Captured using RGB Camera)

The hyperspectral camera used in this paper is a frame-based snapshot camera that covers the green visible spectrum to the NIR spectrum from 500 nm to 900 nm. The camera spectral FWHM is between 6 nm and 18 nm, with a 1 nm spectral resolution. The camera was mounted on a custom-built UAV drone and flew 150 m above the ground to capture the tree's canopy. When capturing each block, the camera will capture it 3 times simultaneously. Each hyperspectral image has a spatial dimension of  $1024 \times 1024$  and consists of 402 spectral dimensions with covert wavelengths of 500 nm to 900 nm. Based on the evaluation results, 48 were identified as Healthy and 21 as Infected. Figure 3 shows the hyperspectral image of the oil palm trees with their ground truths.

#### 3.2. Feature-Based Band Alignment

Frame-based cameras capture a sequence of bands in time, resulting in a time gap between two consecutive spectral bands [35], as shown in Figure 4. To ensure data integrity, the acquisition platform needs to remain stationary during the capturing process, ensuring each band is acquired from the same principal point and with the same geometry [36]. Although the UAV is programmed for a stationary flight over the plant, unavoidable slight motions or movements occur due to sudden strong wind during data acquisition. Figure 5 shows the false RGB image of the captured hyperspectral image, which seems to have a slight misalignment or blurring of the lines and shape. This results in significant displacements between bands, causing the spectral signature of an object to be mixed or corrupted by background or other objects. Therefore, it is essential to apply band alignment before performing any analysis or classification.

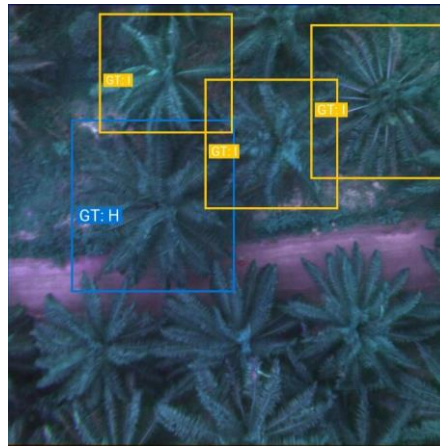


Figure 3. False RGB image (wavelengths: 141 nm, 45 nm, and 196 nm)

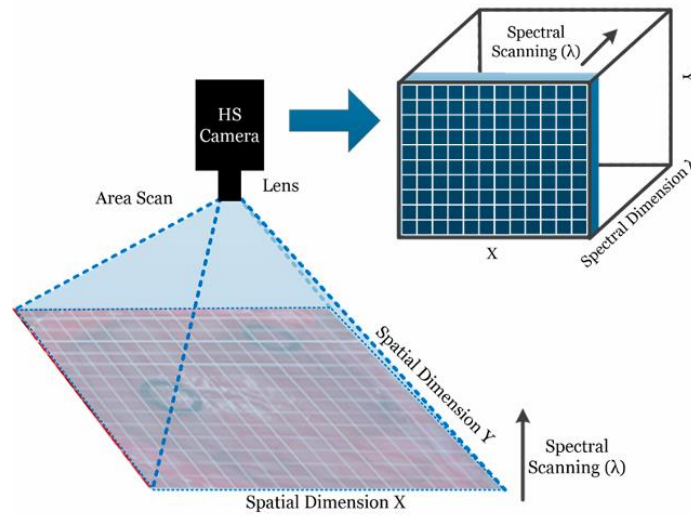


Figure 4. Frame-based hyperspectral camera and its respective acquisition methods from Halicek et al. (2019) [37]

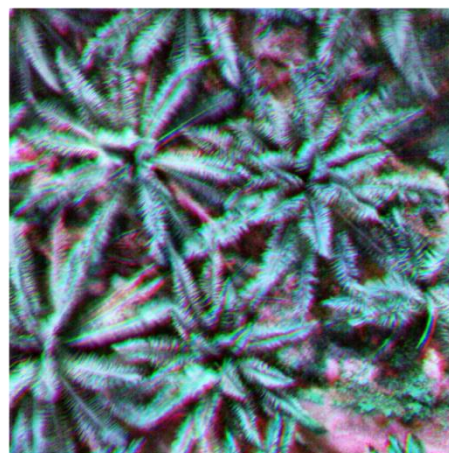


Figure 5. False RGB image with no band alignment (wavelengths: 141 nm, 45 nm, and 196 nm)

To address this misalignment issue, a feature-based hyperspectral band alignment is proposed to align the images. The proposed band alignment flowchart, shown in Figure 6, utilizes a pairwise approach to align bands sequentially. The first band serves as a reference to align the second band, which is considered the target. To facilitate feature extraction using the Scale-Invariant Feature Transform (SIFT) algorithm [38], both the reference and target bands are converted to grayscale images using Equation 1. Since there may be significant changes in illumination between each band, histogram equalization is applied to adjust contrast using the image’s histogram.

$$Grayscale = \frac{Band - \min(Band)}{\max(Band) - \min(Band)} \times 255 \tag{1}$$

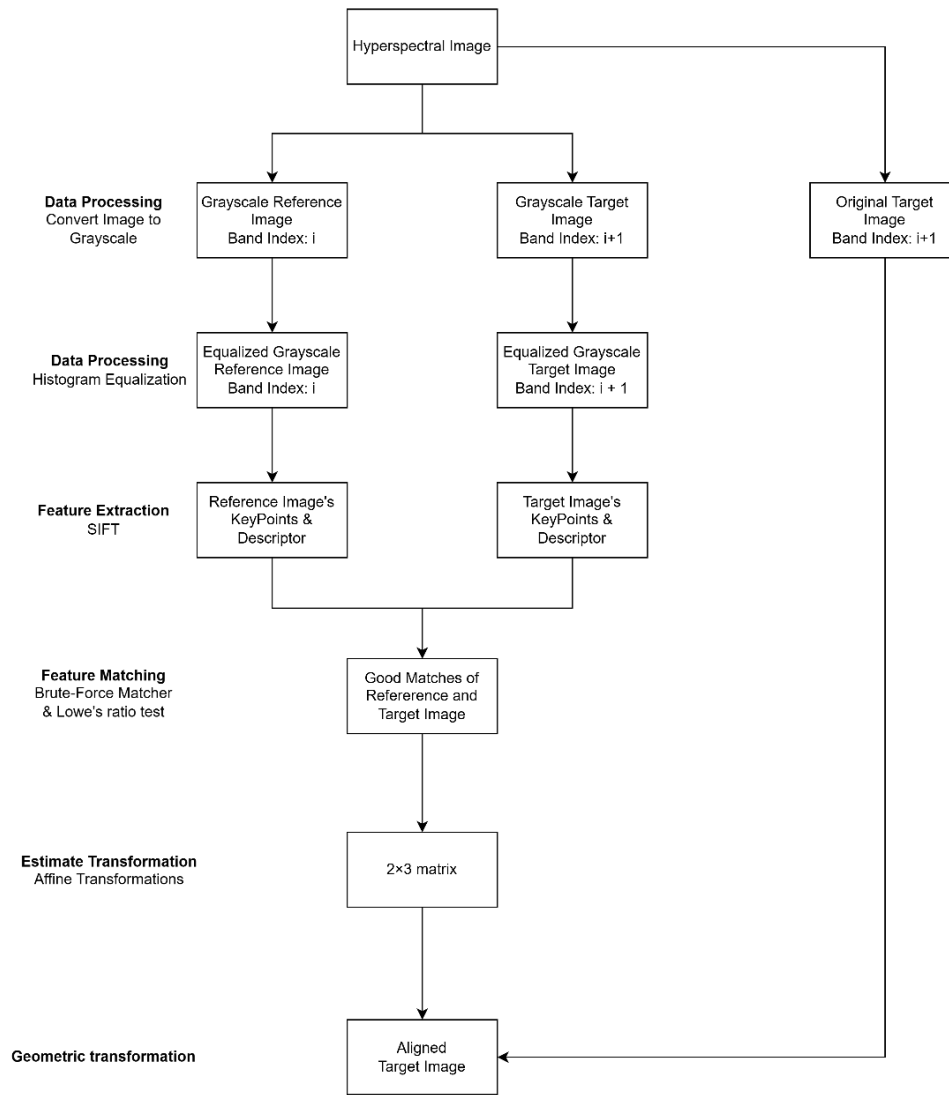


Figure 6. Flowchart of the band alignment method

The SIFT algorithm is then applied to the histogram equalized images, generating features consisting of key points and descriptors. Each feature includes the key points and descriptors. Subsequently, feature matching is conducted to establish correspondence between key points in different images by applying a brute-force matcher and Lowe’s ratio test. The resulting inliers from the ratio test estimate a transformation matrix through affine transformation, which combines linear transformations (rotation, scaling, shearing) and translation (shifting). Once obtained, this transformation matrix, representing the geometric relationship between the reference and target bands, is then applied to the original target band (not the grayscale image) to perform the geometric transformation and align it with the reference band. This iterative process continues, using the aligned band as a reference until all bands are aligned. Figure 7 shows the differences between the images with and without alignment.

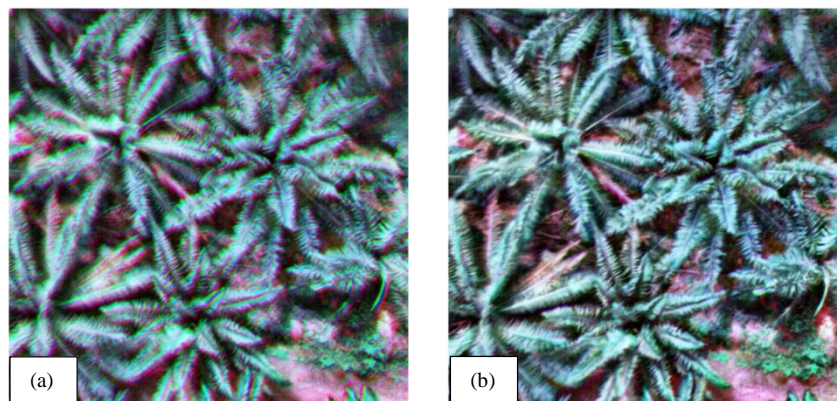


Figure 7. False RGB image of the hyperspectral images (wavelengths: 141 nm, 45 nm, 196 nm): (a) before band alignment, (b) after band alignment

To evaluate the accuracy of the proposed band alignment method, the alignment accuracy between adjacent band pairs upon alignment is estimated using Root-Mean-Square Error (RMSE), Pearson Correlation Coefficient (PCC), and Normalized Mutual Information (NMI). The lower value of RMSE indicates the better alignment accuracy of the proposed alignment. The RMSE is calculated by using the matched key points between the reference band and the target band using Equation 2. In Equation 2,  $r$  refers to the reference band,  $t$  refers to the target band, and  $n$  represents the total number of matched key points. Each key point is a set of  $x$  and  $y$  pixel coordinates representing the location of a feature in the band. A lower RMSE value indicates less residual variance and better accuracy of the alignment.

$$RMSE_{r,t} = \sqrt{\frac{\sum_{i=1}^n (x_{r_i} - x_{t_i})^2 + (y_{r_i} - y_{t_i})^2}{n}} \quad (2)$$

The Pearson Correlation Coefficient (PCC) [39] measures the linear relationship between the two bands, which can be used to evaluate the accuracy of the alignment. The equation of  $PCC$  value between bands shown in Equation 3. In Equation 3,  $r$  refers to the reference band,  $t$  refers to the target band,  $W$  and  $H$  refer to the width and the height of the hyperspectral image.  $\overline{r_{x,y}}$  and  $\overline{t_{x,y}}$  refer to the mean of  $r_{x,y}$  and  $t_{x,y}$  as shown in Equations 4 and 5, respectively.

$$PCC_{r,t} = \frac{\sum_{x=1,y=1}^{x=W,y=H} (r_{x,y} - \overline{r_{x,y}})(t_{x,y} - \overline{t_{x,y}})}{\sqrt{\sum_{x=1,y=1}^{x=W,y=H} (r_{x,y} - \overline{r_{x,y}})^2 * \sum_{x=1,y=1}^{x=W,y=H} (t_{x,y} - \overline{t_{x,y}})^2}} \quad (3)$$

$$\overline{r_{x,y}} = \frac{\sum_{x=1,y=1}^{x=W,y=H} r_{x,y}}{W * H} \quad (4)$$

$$\overline{t_{x,y}} = \frac{\sum_{x=1,y=1}^{x=W,y=H} t_{x,y}}{W * H} \quad (5)$$

The Normalized Mutual Information (NMI) [40] measures the relationship between the pixel intensities in the two bands. It could effectively measure the alignment quality, especially presence of noise or complex intensity relationships. The equation of the NMI is shown in Equation 6. In the equation,  $r$  refers to the reference band while  $t$  refers to the target band.  $H(r)$  and  $H(t)$  are marginal entropies which are calculated using Equation 7.  $H(r, t)$  is the joint entropy which is calculated using Equation 8.

$$NMI_{r,t} = \frac{H(r) + H(t)}{H(r, t)} \quad (6)$$

$$H(I) = - \sum_{i \in I} P(i) * \log(P(i)) \quad (7)$$

$$H(r, t) = - \sum_{i \in r} \sum_{j \in t} P(i, j) * \log(P(i, j)) \quad (8)$$

To evaluate the performance of the hyperspectral image,  $\overline{RMSE}$ ,  $\overline{PCC}$ , and  $\overline{NMI}$  are calculated by using Equations 9 to 11, respectively. The equations averaging all the value of the align accuracy between adjacent band pairs, which calculated  $b - 1$  times. In the equations,  $b$  refers to the number of bands in the hyperspectral image.

$$\overline{RMSE} = \frac{\sum_{i=2}^{b-1} RMSE_{i-1,i}}{b-1} \quad (9)$$

$$\overline{PCC} = \frac{\sum_{i=2}^{b-1} PCC_{i-1,i}}{b-1} \quad (10)$$

$$\overline{NMI} = \frac{\sum_{i=2}^{b-1} NMI_{i-1,i}}{b-1} \quad (11)$$

### 3.3. Denoise

After the data cube's bands are aligned, the spectral signature of a pixel shows there is still some peak noise in the hyperspectral data cube. Therefore, a pixel-based Savitzky-Golay smoothing filter is used to smooth out the spectral signature [41]. The comparison of spectral signature before and after the filtering is shown in Figure 8.

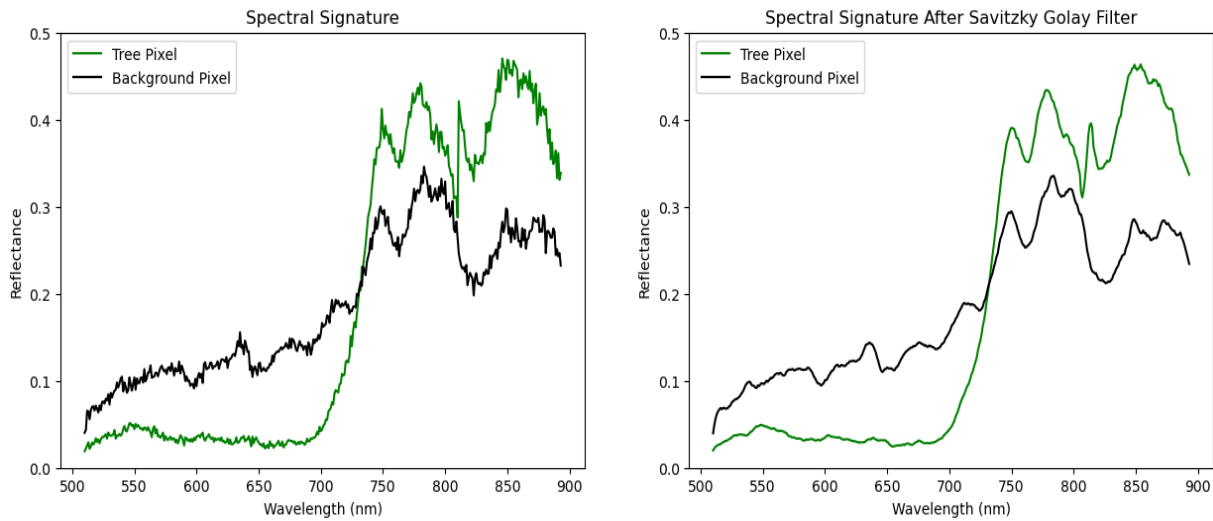


Figure 8. The spectral signature before Savitzky-Golay smoothing filter (left) and after Savitzky-Golay smoothing filter (right)

### 3.4. Background Subtraction

Removing background noise from the hyperspectral images is important before generating a spectral representation dataset suitable for machine learning. This is because individual trees are cropped out from the image during the conversion of hyperspectral images into a tabular form of spectral representation (details will be explained in the following subsection). Still, these cropped tree images often contain information about other objects, such as soil, different vegetation, and shadows. This extraneous information can interfere with the accurate analysis of spectral signatures from oil palm trees, potentially leading to inaccurate representation in the tabular dataset and impacting the performance of the machine learning models. A background subtraction method is implemented to tackle this issue, which utilizes K-means clustering to cluster oil palm trees and other objects based on spectral signature differences.

Before performing clustering, principal component analysis (PCA) is used to reduce the dimensionality of the hyperspectral image while keeping the explained variance to 95%, allowing K-means to cluster the pixels more effectively without losing much spectral information. The K-means clustering then utilizes dimension-reduced hyperspectral images and groups pixels based on spectral similarity, separating the tree pixels from the background pixels with distinct spectral properties—the K-means clustering groups pixels into two classes: tree pixels and background pixels. As K-means is an unsupervised learning method, the classes might differ from the desired outcome classes. To overcome this issue, the classes will be reassigned to the desired outcome classes by checking the spectral signature of the oil palm tree and background, as the value of the background’s spectral signature is lower than the value of the oil palm tree’s spectral signature. The spectral signature of the oil palm tree and background are shown in Figure 9. The result of the background subtraction is shown in Figure 10.

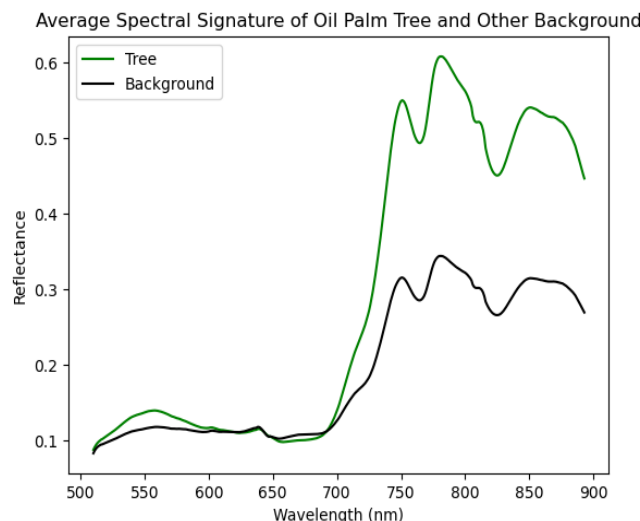


Figure 9. Spectral signature comparison of oil palm and background

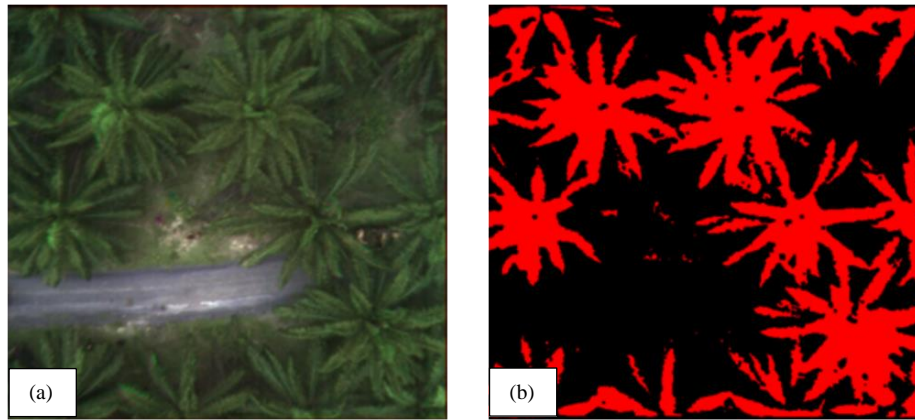


Figure 10. Background subtraction result: (a) false RGB hyperspectral image; (b) background subtracted mask

To evaluate the effectiveness of the background subtraction, the Intersection over Union (IoU), Dice Similarity Coefficient (DSC), and precision were employed using the ground truth of the hyperspectral images annotated manually using Computer Vision Annotation Tool (CVAT) (CVAT.ai Corporation, 2023: *Computer software*). Retrieved from <https://github.com/cvat-ai/cvat>. The IoU provided insights into the segmentation performance and captured the spatial extent of potentially desired regions. It allows us to describe how well the proportions of the segmented tree region overlap with the actual region. On the other hand, DSC, like IoU, is given more weight to segment tree areas correctly and penalizes tree areas that are under segmentation. DSC emphasizes the accurate overlap over the pure region size segment. Precision is used to evaluate how many tree pixels are classified as trees. The formulas of the IoU, DSC, and precision are shown in Equations 12 to 14, respectively.

$$IoU = \frac{True\ Positives}{True\ Positives + False\ Positives + False\ Negatives} \tag{12}$$

$$DSC = \frac{2 * True\ Positives}{2 * True\ Positives + False\ Positives + False\ Negatives} \tag{13}$$

$$Precision = \frac{True\ Positives}{True\ Positives + False\ Positives} \tag{14}$$

### 3.5. Prediction

The images are converted into a tabular form of spectral representation to utilize only spectral information of hyperspectral images. The process is illustrated in Figure 11. Once all the hyperspectral images are band-aligned and denoised, the background of the hyperspectral images is removed using the implemented background subtraction method. It ensures that the spectral representation dataset accurately reflects the spectral characteristics of the oil palm trees and minimizes the influence of irrelevant spectral information. Then, the images of trees are annotated using the CVAT annotation tool. Based on the annotation, the trees are cropped from their background-subtracted hyperspectral image. Since each tree’s spatial dimension differs, all cropped tree images are fixed to a spatial dimension of 500 × 500 by adding zero paddings. After processing all images, the cropped tree samples are merged into the cropped dataset.

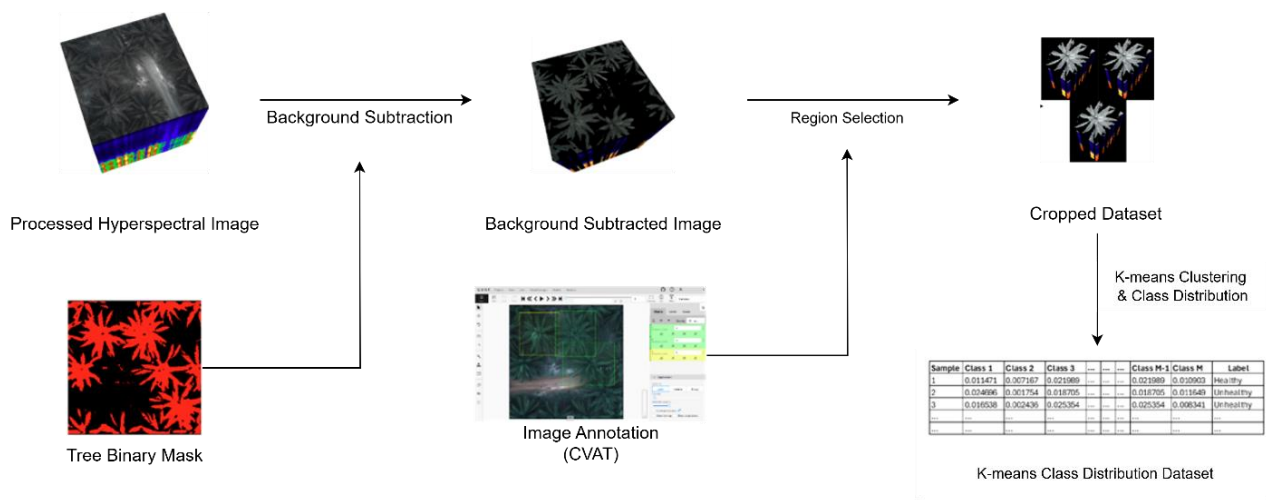


Figure 11. Dataset Process Flow

Afterwards, the Cropped Dataset is used to train a K-means clustering, which clusters the tree pixels into 15 classes. Once trained, all the tree samples are used as K-means input to predict their classification map. A classification map is an image representation that assigns different clustered classes to distinct pixels within tree samples based on the K-means model prediction. These classification maps make up the K-means Cluster Map Dataset. To organize and present this distribution information in a structured manner, the K-means Cluster Map Dataset is converted into a tabular format called the Pixel Classes Distribution Dataset. Each row in the table represents a region of interest within the image, and columns correspond to the different classes. The entries in the table indicate the frequency or proportion of each class within the corresponding region.

Finally, with the hyperspectral data transformed into a tabular format represented by the Pixel Classes Distribution Dataset, four different machine learning classifiers are employed to distinguish between healthy and *Ganoderma* infected oil palm trees: Support Vector Machine (SVM) with several kernels (i.e., linear, polynomial, sigmoid, and radial basis function), Random Forest (RF), Multilayer Perceptron (MLP), and Decision Tree (DT). Using a stratified sampling approach, the dataset is split into a train set (70%) and a test set (30%). This ensures that train and test subsets have the same class distribution in the original dataset, eliminating the class imbalance issue. Each method was employed under the same parameter settings and dataset to ensure a fair and valid comparison of classifiers' performance.

Several evaluation metrics for the model performance evaluation include accuracy, specificity, sensitivity, and Cohen's Kappa Coefficient. Accuracy provides a general indication of the model's performance by measuring the number of samples correctly classified across the entire dataset, providing the overall correctness of the rule-based model. Sensitivity, also known as recall, measures how well the model can classify infected trees, which are true positives. Sensitivity is the most important metric, as it indicates the model's ability to detect *Ganoderma* disease effectively. A high sensitivity score is essential to ensure that infected trees are not missed, allowing for timely intervention. Specificity, also known as recall, measures how well the model can classify healthy trees, which are true negatives. A high specificity score indicates the model has low false positives, as incorrectly classifying healthy trees could lead to unnecessary treatments and resource allocation. Cohen's Kappa Coefficient measures the model's reliability in classification tasks. It provides a more reliable measure of the model's performance than simple accuracy, especially when dealing with imbalanced datasets. The equations of accuracy, specificity, sensitivity, and Cohen's Kappa Coefficient are used in Equations 15 to 18, respectively.

$$Accuracy = \frac{True\ Positives + True\ Negatives}{Total\ Samples} \quad (15)$$

$$Specificity = \frac{True\ Negatives}{True\ Negatives + False\ Positives} \quad (16)$$

$$Sensitivity = \frac{True\ Positives}{True\ Positives + False\ Negatives} \quad (17)$$

$$K = \frac{p_o - p_e}{1 - p_e} \quad (18)$$

## 4. Discussion and Experiment Results

### 4.1. Band Alignment

For the evaluation of the band alignment method, the hyperparameters used in the SIFT ratio test are fixed, as shown in Table 3. The results of the three proposed evaluation metrics (RMSE, PCC, and NMI) calculated for adjacent band pairs are presented in Figures 12 to 14, respectively. Based on the figures, it's evident that for most adjacent band pairs, there is a significant improvement in alignment after applying the band alignment method. The accuracy of the alignment on the hyperspectral image is shown in Table 4. Comparing the band alignment hyperspectral image with the raw hyperspectral image, it shows 79.5%, 0.7%, and 7.2% improvement on  $\overline{RMSE}$ ,  $\overline{PCC}$ , and  $\overline{NMI}$ , respectively. These results demonstrate that the proposed band alignment method significantly minimizes spectral misalignment in hyperspectral images.

**Table 3. Evaluation of developed band alignment method**

Function/ Class	Hyperparameter	Value
SIFT	nfeatures	1000000000
BFMatcher.knnMatch()	k	2
Lowe's Ratio Test	threshold	0.7

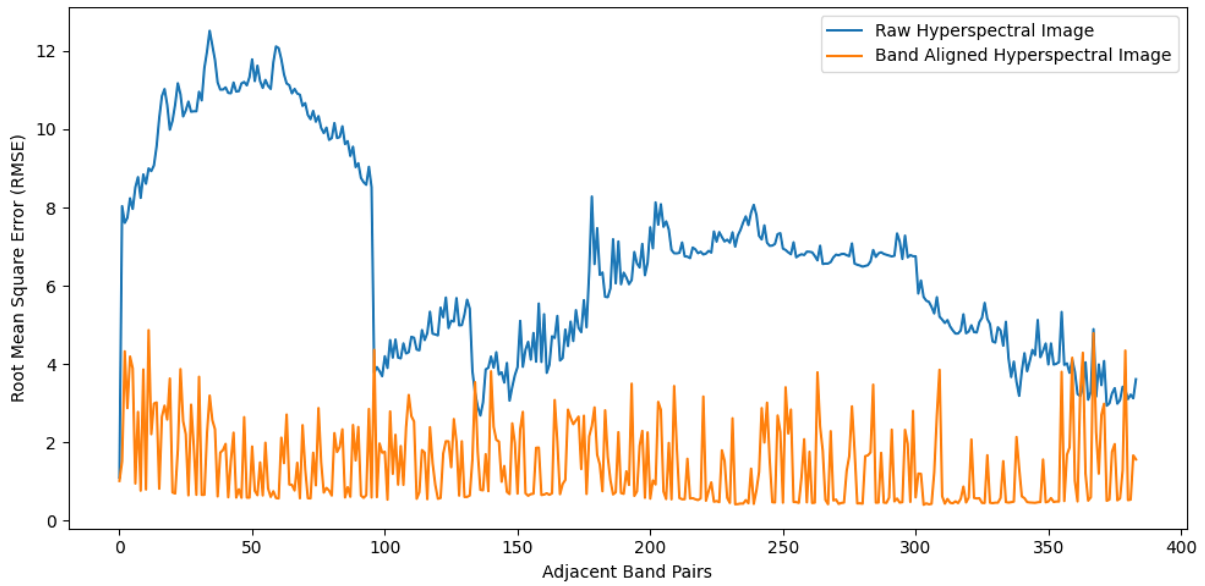


Figure 12. Comparison of RMSE for adjacent band pairs in raw and aligned hyperspectral images

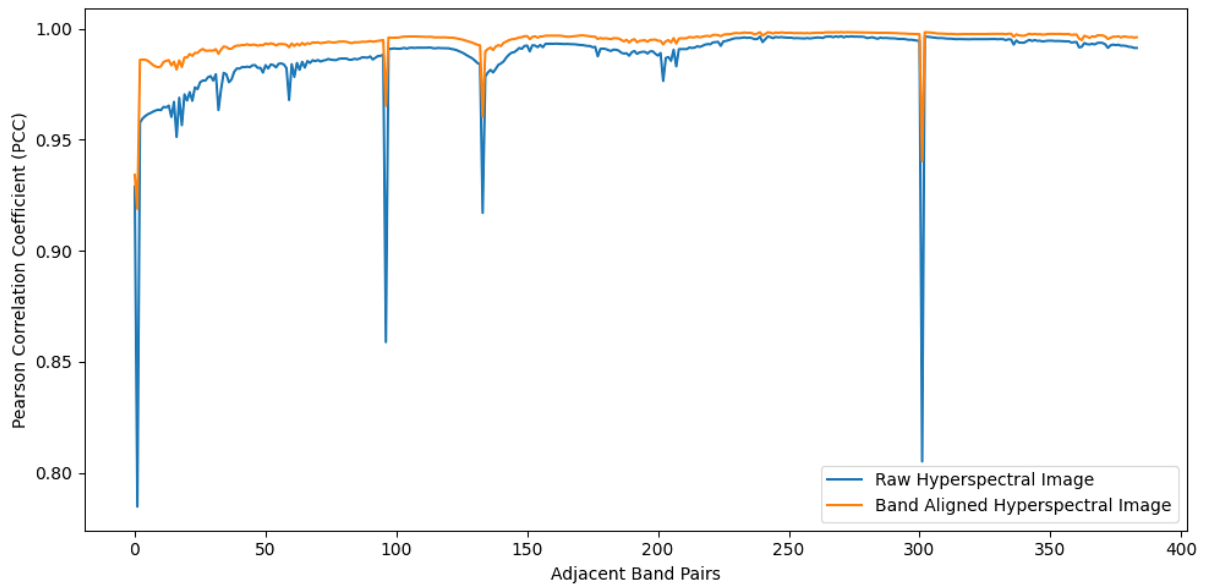


Figure 13. Comparison of PCC for adjacent band pairs in raw and aligned hyperspectral images

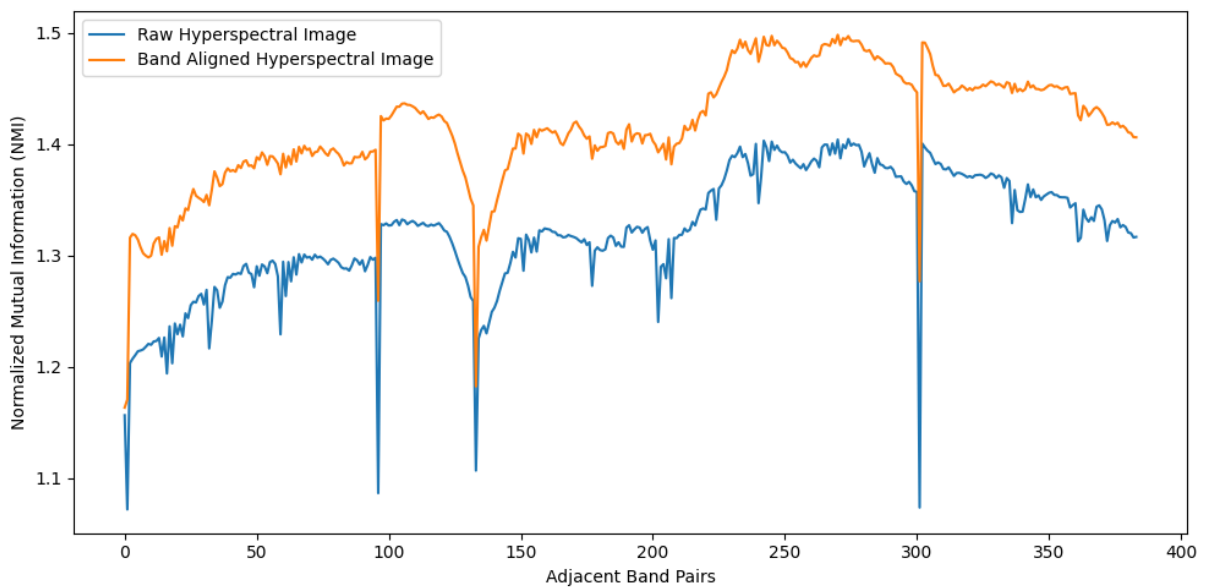


Figure 14. Comparison of NMI for adjacent band pairs in raw and aligned hyperspectral images

**Table 4. Evaluation of developed band alignment method**

Metrics	Higher/Lower Better	Raw Hyperspectral Image	Aligned Hyperspectral Image	Differences (% , Absolute Value)
$\overline{RMSE}$	Lower	6.8580	1.4043	79.5%
$\overline{PCC}$	Higher	0.9875	0.9946	0.7%
$\overline{NMI}$	Higher	1.3213	1.4165	7.2%

#### 4.2. Background Subtraction

Tree region-level precision is used as the primary metric to assess segmentation performance with a strong emphasis on minimizing the misclassification of background pixels. This metric directly reflects the proportion of correctly identified tree pixels from all labeled 'trees' in the segmentation output. The developed background subtraction method achieved a precision score of 93.99%, indicating that the model can select tree regions significantly while effectively minimizing the background pixels wrongly classified as 'background'. This result suggests that the developed background subtraction method fulfilled the main requirement for accurate background removal.

For the overlap-based metric, the Intersection over Union (IoU) and Dice Similarity Coefficient (DSC) scored 0.6278 and 0.7702, respectively. Based on the result, the Intersection over Union (IoU) score suggests that the model accurately identifies the core areas of trees. Still, it may exhibit some limitations in perfectly capturing the full spatial extent of every tree crown, potentially leading to minor under-segmentation. The relatively higher DSC compared to IoU suggests that while there might be minor discrepancies in boundary delineation, the model excels at capturing the truest tree pixels. The results of these metrics show that the developed method can accurately identify tree pixels. However, as suggested by the IoU and DSC values, further refinement might be beneficial to improve the technique to allow complete boundary contours of the tree regions. Table 5 summarizes the results of the metrics.

**Table 5. Evaluation of developed background subtraction method**

Metrics	Score
Precision	93.99%
IoU	0.6278
DSC	0.7702

#### 4.3. Prediction Result

The performance of each classifier is presented in Table 6, where models are evaluated using four metrics: accuracy, sensitivity, specificity, and Cohen's Kappa coefficient. The Multilayer Perceptron (MLP) model demonstrated exceptional performance with 100% accuracy, sensitivity, and specificity, achieving a Cohen's Kappa coefficient of 1.00. This remarkable performance highlights the model's ability to capture the nonlinear relationships in the data and effectively distinguish delicate patterns within the limited feature space that distinguishes infected trees from healthy ones. However, this raises concerns of potential overfitting, as given limited samples, the model may have simply memorized the training data instead of learning generalized patterns. While this performance is promising, further validation with a larger, more diverse dataset is crucial to assess the MLP's true generalizability and mitigate potential overfitting concerns.

**Table 6. Evaluation of developed background subtraction method**

Methods	Accuracy (%)	Sensitivity (%)	Specificity (%)	Cogen's Kappa Coefficient
MLP	100.00	100.00	100.00	1.00
SVM (RBF)	91.67	83.33	100.00	0.8333
SVM (Polynomial)	91.67	83.33	100.00	0.8333
SVM (Sigmoid)	66.67	50.00	83.33	0.3333
SVM (Linear)	66.67	83.33	50.00	0.3333
Random Forest	83.33	66.67	100.00	0.6667
Decision Tree	62.50	100.00	25.00	0.2500

The Support Vector Machine (SVM) with radial basis function (RBF) and polynomial kernels achieved an accuracy of 91.67%, a specificity of 100%, and a Kappa score of 0.8333, but they both with a lower sensitivity score of 83.33%. This indicates that these SVM models can accurately identify healthy trees, but they may miss some infected trees, suggesting potential limitations in detecting subtle spectral variations associated with early infection stages. On the other hand, SVM with Sigmoid kernel achieved a lower performance of 66.67% accuracy, 50% sensitivity, 83.33% specificity, and 0.3333 kappa score. This performance suggests that the linear and sigmoid kernels might not be as effective in capturing the non-linear relationships present in the spectral data of oil palm trees.

The Random Forest (RF) model achieved an accuracy of 83.33%, a sensitivity of 66.67%, a specificity of 100%, and a Kappa score of 0.6667. The RF model demonstrated proficiency in identifying healthy trees but exhibited limitations in detecting all infected trees, suggesting potential challenges in capturing the full range of spectral variations associated with *Ganoderma* infection. The Decision Tree (DT) model obtained an accuracy of 62.50%, a specificity of 25.00%, and a Kappa score of 0.2500. However, it displayed a high sensitivity of 100%, indicating its potential to identify all infected trees. This suggests that while the DT model may not be as accurate overall, it excels at recognizing infected trees, even in early stages when subtle spectral changes might be present.

## 5. Conclusion

This study presents a *Ganoderma* disease detection on oil palm trees approach using hyperspectral imaging and machine learning techniques. To overcome the hyperspectral image misalignment, a feature-based band alignment method is developed to enhance the accuracy of spectral data. The result significantly improves spectral coherence across adjacent bands, quantified by RMSE, PCC, and NMI metrics. The background subtraction was also developed to isolate tree pixels and eliminate irrelevant spectral information. Based on a 93.99% precision score, the developed method can eliminate most of the background. However, IoU and DSC suggested that future improvement is required to capture the full spatial extent of the trees. Future improvements will focus on improving the boundary delineation to allow complete boundary contours of the tree regions.

Using an MLP classifier on features extracted from clustered pixel classes, the prediction model exhibited exceptional performance with 100% accuracy, sensitivity, and specificity. This perfect score suggests the model's efficacy but highlights the need for further validation with a larger, more diverse dataset to confirm generalizability and address potential overfitting concerns.

Future research will involve collecting datasets, including temporal information, for enhanced disease stage classification. In terms of the prediction model, future studies can explore other machine-learning techniques to improve the prediction accuracy. Overall, this study utilizes hyperspectral imaging as a powerful tool for accurately detecting *Ganoderma* disease in oil palm plantations.

## 6. Declarations

### 6.1. Author Contributions

Conceptualisation, K.C.S. and M.Z.A.Z.; methodology, K.C.S.; validation, M.K.A.M. and H.A.; formal analysis, K.C.S., T.H.T., and M.Z.A.Z.; investigation, K.C.S., S.F.A.R., and S.Y.; resources, T.T.H., M.K.A.M., and H.A.; writing—original draft preparation, K.C.S., S.F.A.R., and S.Y.; writing—review and editing, K.C.S., S.F.A.R., and S.Y. All authors have read and agreed to the published version of the manuscript.

### 6.2. Data Availability Statement

The data presented in this study are available on request from the corresponding author.

### 6.3. Funding

The authors received no financial support for the research, authorship, and/or publication of this article.

### 6.4. Acknowledgments

The authors sincerely thank FGV R&D Sdn Bhd and iRadar Sdn Bhd for their generous support in providing valuable data and resources for this study. We acknowledge that the successful completion of this project was facilitated by their valuable contribution, allowing for in-depth analysis of hyperspectral images. Moreover, we appreciate the efforts of our collaborators, whose technical expertise has been instrumental to the development and success of the project.

### 6.5. Institutional Review Board Statement

Not Applicable.

### 6.6. Informed Consent Statement

Not applicable.

### 6.7. Declaration of Competing Interest

The authors declare that there are no conflicts of interest concerning the publication of this manuscript. Furthermore, all ethical considerations, including plagiarism, informed consent, misconduct, data fabrication and/or falsification, double publication and/or submission, and redundancies have been completely observed by the authors.

## 7. References

- [1] Kaniapan, S., Hassan, S., Ya, H., Nesan, K. P., & Azeem, M. (2021). The utilisation of palm oil and oil palm residues and the related challenges as a sustainable alternative in biofuel, bioenergy, and transportation sector: A review. *Sustainability (Switzerland)*, 13(6), 3110. doi:10.3390/su13063110.
- [2] Ahmad, M. J., Ismail, R., & Ghani, F. A. (2023). Review on socioeconomic and sustainability of oil palm plantations among rural communities in Malaysia. *IOP Conference Series: Earth and Environmental Science*, 1208(1), 12054. doi:10.1088/1755-1315/1208/1/012054.
- [3] Parveez, G. K. A., Rasid, O. A., Ahmad, M. N., Taib, H. M., Bakri, M. A. M., Hafid, S. R. A., Tuan Ismail, T. N. M., Loh, S. K., Abdullah, M. O., Zakaria, K., & Idris, Z. (2023). Oil Palm Economic Performance in Malaysia and R&D Progress in 2022. *Journal of Oil Palm Research*, 35(2), 193–216. doi:10.21894/jopr.2023.0028.
- [4] Izzuddin, M. A., Ezzati, B., Nisfariza, M. N., Idris, A. S., & Alias, S. A. (2019). Analysis of red, green, blue (RGB) and near infrared (NIR) images from unmanned aerial vehicle (UAV) for detection of Ganoderma disease in oil palm. *Oil Palm Bull*, 79, 9-15.
- [5] Roslan, A., & Idris, A. S. (2012). Economic impact of Ganoderma incidence on Malaysian oil palm plantation—a case study in Johor. *Oil Palm Industry Economic Journal*, 12(1), 24-30.
- [6] Chong, K.P., Dayou, J., Alexander, A. (2017). Pathogenic Nature of Ganoderma boninense and Basal Stem Rot Disease. Detection and Control of Ganoderma boninense in Oil Palm Crop. *SpringerBriefs in Agriculture*. Springer, Cham, Switzerland. doi:10.1007/978-3-319-54969-9\_2.
- [7] Ahmadi, P., Mansor, S., Farjad, B., & Ghaderpour, E. (2022). Unmanned Aerial Vehicle (UAV)-Based Remote Sensing for Early-Stage Detection of Ganoderma. *Remote Sensing*, 14(5), 1239. doi:10.3390/rs14051239.
- [8] Hushiarian, R., Yusof, N. A., & Dutse, S. W. (2013). Detection and control of Ganoderma boninense: Strategies and perspectives. *SpringerPlus*, 2(1), 1–12. doi:10.1186/2193-1801-2-555.
- [9] Pilotti, C. A., Gorea, E. A., & Bonneau, L. (2018). Basidiospores as sources of inoculum in the spread of Ganoderma boninense in oil palm plantations in Papua New Guinea. *Plant Pathology*, 67(9), 1841–1849. doi:10.1111/ppa.12915.
- [10] Hendra, H., Haryadi, D., Sidhu, M., Samosir, Y., & Tan, J. S. (2024). Comparative incidence of Ganoderma basal stem rot and upper stem rot disease in oil palm in relation to soil type and geographical distribution. *IOP Conference Series: Earth and Environmental Science*, 1308(1), 12016. doi:10.1088/1755-1315/1308/1/012016.
- [11] Rakib, M. R. M., Clament, C. F. S., Dayang Syazanie, A. E., & Darwana, D. (2020). Investigation on Ganoderma infection in oil palm based on the cultural characteristics and somatic compatibility: A case study in Sandakan, Sabah. *ASM Science Journal*, 13(6), 23–29.
- [12] Izzuddin, M. A., Hamzah, A., Nisfariza, M. N., & Idris, A. S. (2020). Analysis of multispectral imagery from unmanned aerial vehicle (UAV) using object-based image analysis for detection of Ganoderma disease in oil palm. *Journal of Oil Palm Research*, 32(3), 497–508. doi:10.21894/jopr.2020.0035.
- [13] Anuar, I. M., Arof, H. bin, Mohd Nor, N. binti, Hashim, Z. bin, Abu Seman, I. bin, Masri, M. M., Ibrahim, S. M., Tat, E. H., & Toh, C. M. (2021). Remote Sensing for Detection of Ganoderma Disease and Bagworm Infestation in Oil Palm. *Advances in Agricultural and Food Research Journal*, 2(1), 1-14. doi:10.36877/aafj.a0000189.
- [14] Husin, N. A., Khairunniza-Bejo, S., Abdullah, A. F., Kassim, M. S. M., Ahmad, D., & Aziz, M. H. A. (2020). Classification of basal stem rot disease in oil palm plantations using terrestrial laser scanning data and machine learning. *Agronomy*, 10(11), 1624. doi:10.3390/agronomy10111624.
- [15] Khairunniza-Bejo, S., Shahibullah, M. S., Azmi, A. N. N., & Jahari, M. (2021). Non-destructive detection of asymptomatic ganoderma boninense infection of oil palm seedlings using nir-hyperspectral data and support vector machine. *Applied Sciences (Switzerland)*, 11(22), 10878. doi:10.3390/app112210878.
- [16] Azmi, A. N. N., Bejo, S. K., Jahari, M., Muharam, F. M., Yule, I., & Husin, N. A. (2020). Early detection of Ganoderma boninense in oil palm seedlings using support vector machines. *Remote Sensing*, 12(23), 1–21. doi:10.3390/rs12233920.
- [17] Ahmadi, P., Muharam, F. M., Ahmad, K., Mansor, S., & Seman, I. A. (2017). Early detection of ganoderma basal stem rot of oil palms using artificial neural network spectral analysis. *Plant Disease*, 101(6), 1009–1016. doi:10.1094/PDIS-12-16-1699-RE.
- [18] Lelong, C. C. D., Roger, J.-M., Bregand, S., Dubertret, F., Lanore, M., Sitorus, N. A., Raharjo, D. A., & Caliman, J.-P. (2009). Discrimination of fungal disease infestation in oil-palm canopy hyperspectral reflectance data. 2009 First Workshop on Hyperspectral Image and Signal Processing: Evolution in Remote Sensing, 1–4. doi:10.1109/whispers.2009.5289017.
- [19] Shafri, H. Z. M., Anuar, M. I., & Saripan, M. I. (2009). Modified vegetation indices for Ganoderma disease detection in oil palm from field spectroradiometer data. *Journal of Applied Remote Sensing*, 3(1), 033556.
- [20] Izzuddin, M. A., Seman Idris, A., Nisfariza, M. N., Nordiana, A. A., Shafri, H. Z. M., & Ezzati, B. (2017). The development of spectral indices for early detection of Ganoderma disease in oil palm seedlings. *International Journal of Remote Sensing*, 38(23), 6505–6527. doi:10.1080/01431161.2017.1335908.

- [21] Liaghat, S., Ehsani, R., Mansor, S., Shafri, H. Z. M., Meon, S., Sankaran, S., & Azam, S. H. M. N. (2014). Early detection of basal stem rot disease (Ganoderma) in oil palms based on hyperspectral reflectance data using pattern recognition algorithms. *International Journal of Remote Sensing*, 35(10), 3427–3439. doi:10.1080/01431161.2014.903353.
- [22] Tan, M. I. S. M. H., Jamlos, M. F., Omar, A. F., Kamarudin, K., & Jamlos, M. A. (2023). Ganoderma boninense classification based on near-infrared spectral data using machine learning techniques. *Chemometrics and Intelligent Laboratory Systems*, 232. doi:10.1016/j.chemolab.2022.104718.
- [23] Liaghat, S., Mansor, S., Ehsani, R., Shafri, H. Z. M., Meon, S., & Sankaran, S. (2014). Mid-infrared spectroscopy for early detection of basal stem rot disease in oil palm. *Computers and Electronics in Agriculture*, 101, 48–54. doi:10.1016/j.compag.2013.12.012.
- [24] Hermantoro, Kurniawan, M. A., Trinugroho, J. P., Suparyanto, T., Isnain, M., Sudigyo, D., & Pardamean, B. (2023). Detecting Ganoderma Basal Stem Rot Disease on Oil Palm Using Artificial Neural Network Method. *Communications in Mathematical Biology and Neuroscience*, 7911. doi:10.28919/cmbn/7911.
- [25] Johari, S. N. Á. M., Bejo, S. K., Lajis, G. A., DaimDai, L. D. J., Keat, N. B., Ci, Y. Y., & Ithnin, N. (2021). Detecting BSR-infected Oil Palm Seedlings using Thermal Imaging Technique. *Basrah Journal of Agricultural Sciences*, 34, 73–80. doi:10.37077/25200860.2021.34.sp1.8.
- [26] Hashim, I. C., Shariff, A. R. M., Bejo, S. K., Muharam, F. M., & Ahmad, K. (2021). Classification of non-infected and infected with basal stem rot disease using thermal images and imbalanced data approach. *Agronomy*, 11(12), 2373. doi:10.3390/agronomy11122373.
- [27] Wiratmoko, D., Prasetyo, A. E., Jatmiko, R. H., Yusuf, M. A., & Rahutomo, S. (2018). Identification of Ganoderma boninense infection levels on oil palm using vegetation index. *International Journal of Oil Palm*, 1(3), 110–120.
- [28] Ahmadi, P., Mansor, S. B., Ahmadzadeh Araj, H., & Lu, B. (2023). Convolutional SVM Networks for Detection of Ganoderma Boninense at Early Stage in Oil Palm Using Uav and Multispectral Pleiades Images. *ISPRS Annals of the Photogrammetry, Remote Sensing and Spatial Information Sciences*, X-4/W1-2022, 25–30. doi:10.5194/isprs-annals-x-4-w1-2022-25-2023.
- [29] Wahyuni, M., Sabrina, T., Mukhlis, & Santoso, H. (2024). Using Machine Learning in Detecting Ganoderma Disease in Oil Palm Plants. *International Journal of Intelligent Systems and Applications in Engineering*, 12(16s), 145–155.
- [30] Handrian, R. D., Trisasongko, B. H., & Panuju, D. R. (2022). Discriminating the Severity of Basal Stem Rot Disease in Oil Palm (*Elaeis guineensis* Jacq.) Plantation Using Sentinel-2. *IOP Conference Series: Earth and Environmental Science*, 950(1), 12043. doi:10.1088/1755-1315/950/1/012043.
- [31] Yong, L. Z., Khairunniza-Bejo, S., Jahari, M., & Muharam, F. M. (2023). Automatic Disease Detection of Basal Stem Rot Using Deep Learning and Hyperspectral Imaging. *Agriculture (Switzerland)*, 13(1), 69. doi:10.3390/agriculture13010069.
- [32] Kurihara, J., Koo, V. C., Guey, C. W., Lee, Y. P., & Abidin, H. (2022). Early Detection of Basal Stem Rot Disease in Oil Palm Tree Using Unmanned Aerial Vehicle-Based Hyperspectral Imaging. *Remote Sensing*, 14(3), 799. doi:10.3390/rs14030799.
- [33] Lee, C. C., Koo, V. C., Lim, T. S., Lee, Y. P., & Abidin, H. (2022). A multi-layer perceptron-based approach for early detection of BSR disease in oil palm trees using hyperspectral images. *Heliyon*, 8(4), e9252. doi:10.1016/j.heliyon.2022.e09252.
- [34] Win Kent, O., Weng Chun, T., Lee Choo, T., & Weng Kin, L. (2023). Early symptom detection of basal stem rot disease in oil palm trees using a deep learning approach on UAV images. *Computers and Electronics in Agriculture*, 213, 108192. doi:10.1016/j.compag.2023.108192.
- [35] Aasen, H., Honkavaara, E., Lucieer, A., & Zarco-Tejada, P. J. (2018). Quantitative remote sensing at ultra-high resolution with UAV spectroscopy: A review of sensor technology, measurement procedures, and data correction workflows. *Remote Sensing*, 10(7), 1091. doi:10.3390/rs10071091.
- [36] Vakalopoulou, M., & Karantzalos, K. (2014). Automatic descriptor-based co-registration of frame hyperspectral data. *Remote Sensing*, 6(4), 3409–3426. doi:10.3390/rs6043409.
- [37] Halicek, M., Fabelo, H., Ortega, S., Callico, G. M., & Fei, B. (2019). In-vivo and ex-vivo tissue analysis through hyperspectral imaging techniques: Revealing the invisible features of cancer. *Cancers*, 11(6), 756. doi:10.3390/cancers11060756.
- [38] Lowe, D. G. (2004). Distinctive image features from scale-invariant keypoints. *International Journal of Computer Vision*, 60(2), 91–110. doi:10.1023/B:VISI.0000029664.99615.94.
- [39] Pearson, K. (1896). VII. Mathematical contributions to the theory of evolution.—III. Regression, heredity, and panmixia. *Philosophical Transactions of the Royal Society of London. Series A, Containing Papers of a Mathematical or Physical Character*, 187, 253–318. doi:10.1098/rsta.1896.0007.
- [40] Studholme, C., Hill, D. L. G., & Hawkes, D. J. (1999). An overlap invariant entropy measure of 3D medical image alignment. *Pattern Recognition*, 32(1), 71–86. doi:10.1016/S0031-3203(98)00091-0.
- [41] Angel, Y. (2021). Monitoring crop development and health using UAV-based hyperspectral imagery and machine learning. PhD Thesis, King Abdullah University of Science and Technology, Thuwal, Kingdom of Saudi Arabia.